JOURNAL OF MATERIALS SCIENCE 29 (1994) 2998 – 3016

Phase distribution and associated mechanical property distribution in silicon carbide particle-reinforced aluminium fabricated by liquid metal infiltration

SHY-WEN LAI, D. D. L. CHUNG
Composite Materials Research Laboratory, State University of New York at Buffalo, Buffalo, NY 14260, USA

The reaction between silicon carbide and aluminium to form silicon and Al_4C_3 in SiC particle-reinforced aluminium fabricated by liquid aluminium infiltration was most severe near the original interface between liquid aluminium and the SiC preform. This resulted in the highest concentration of Al_4C_3 and the lowest concentrations of silicon and SiC in the part of the composite near this interface. In particular, the silicon concentration was highest in the bottom centre of the composite when infiltration occurred from the top, because silicon diffused toward the surrounding aluminium melt before solidification. These non-uniform phase distributions, as measured by X-ray diffraction and differential scanning calorimetry, did not cause any non-uniform shear strength distribution. However, excessive reaction between SiC and aluminium, as observed for an infiltration (=mould=liquid metal) temperature of 780 °C, caused the tensile strength to decrease. In the case where a steel mould was used during infiltration at 780 °C, iron-containing precipitates, such as ternary Al–Fe–Si, were observed in the part of the composite within 5 mm from the above-mentioned interface; their formation was related to the silicon out-diffusion in the form of liquid Al–Si; they caused the shear strength to be lower in this part of the composite; larger such precipitates (up to 100 μm) were observed in the excess aluminium adjacent to the cast composite. For pure aluminium as the infiltrating metal, the optimum infiltration temperature for the highest tensile strength was 700 °C. An infiltration temperature of 670 °C resulted in incomplete infiltration, which was more severe when a steel mould rather than a graphite mould was used because of the higher thermal conductivity of the former.

1. Introduction

Liquid-metal infiltration is one of the most widely used and commercially important methods of metal-matrix composite fabrication. It can be in the form of vacuum infiltration, squeeze casting, pressure casting or variations thereof. Compared to the powder metallurgy (PM) method, liquid-metal infiltration is faster and can take place at lower pressures. However, liquid-metal infiltration involves a liquid metal, which has a front moving into the preform in a certain direction during infiltration. This directional nature of infiltration is in contrast to the non-directional nature of the PM method. In the case where the reinforcement can react with the metal, the directional nature of liquid-metal infiltration means that the reaction is more severe near the edge of the preform where the front starts to move in, as this edge is in contact with the liquid metal for the longest time during infiltration. This non-uniform reaction severity then results in non-uniform phase distributions, which might lead to a non-uniform mechanical property distribution. The main objective of this work was to examine the phase distributions and investigate their effects, if any, on the mechanical property distribution.

Liquid-metal infiltration is directed toward a mould containing the preform. In the case where the mould material can react with the liquid metal, the reaction is obviously most severe in that part of the composite adjacent to the wall of the mould. This situation can be aggravated by the filler–metal reaction, if any. Thus, the contamination from the mould can lead to non-uniform phase distributions, which might lead to a non-uniform mechanical property distribution. A second objective of this work was to investigate these distributions.

Silicon carbide (SiC) particles are the most widely used filler for reinforcing aluminium because of their superior wettability by molten aluminium compared to other ceramics, such as Al_2O_3 and AlN, and their low cost. Silicon carbide particle-reinforced aluminium is characterized by high strength, high modulus, low coefficient of thermal expansion and low density.

0022–2461

These properties make this composite attractive for aerospace structures, electronic packaging and wear-resistant parts. In addition, SiC reacts with aluminium. Therefore, in this work we used silicon carbide particle-reinforced aluminium for studying the phase distributions and mechanical property distributions mentioned above.

The reaction between SiC and aluminium is actually a drawback that adversely affects the ability of the composite to withstand high temperatures [1]. This reaction forms aluminium carbide (Al_4C_3) and silicon [2–10]. Aluminium carbide is brittle and moisture sensitive. Excessive reaction weakens the filler/matrix bonding and damages the silicon carbide. Silicon is less detrimental, but it dissolves in aluminium and can even form an Al–Si eutectic, which contains 12 wt % Si and melts at 577 °C [5]. The melting temperature of the Al/Si eutectic is lower than that of aluminium (660 °C), so the formation of the Al–Si eutectic degrades the ability of the composite to withstand high temperatures. It was also found [11] that the silicon concentration increase in the aluminium matrix decreases the matrix ductility. This, in turn, decreases the tensile strength of the composite because of insufficient local ductility for the composite to reach the maximum strength [1].

The reaction between aluminium and SiC occurs during the fabrication of the aluminium-matrix composite, as well as during heating of the fabricated composite. When the fabrication does not involve liquid aluminium (but just solid aluminium, as in PM), the reaction between aluminium and SiC occurs at each Al/SiC interface, such that the reaction products do not migrate. However, when the fabrication involves liquid aluminium (as in liquid-metal infiltration), the migration of silicon (a reaction product) is possible, leading to non-uniformity in the silicon distribution. The migration had not been previously reported.

In this work, SiC particulate–aluminium matrix composites were fabricated by vacuum infiltration of liquid aluminium into a porous SiC particle preform under an argon pressure. The silicon distribution in the resulting composite and in the excess aluminium cast around the composite, was studied. The effects of the infiltration temperature and the mould material (steel or graphite) on the phase distribution, the mechanical properties and the mechanical property distribution were also investigated. X-ray diffraction (XRD), scanning electron microscopy (SEM) and energy-dispersive X-ray spectrometry (EDAX) were used to observe the crystalline silicon and other precipitates, whereas differential scanning calorimetry (DSC) was used to observe the Al–Si eutectic and other microconstituents. In addition, tensile testing was used to measure the average mechanical properties while scratch testing was used to measure the shear strength distribution, which was then correlated with the phase distributions.

2. Experimental procedure

2.1. Composite fabrication

The SiC particles used were kindly provided by Electro Abrasives, Inc. (1200-W). The SiC particle size ranged from 1–10 μm, with a mean at 3 μm. The properties of the SiC powder are listed in Table I. The composition of SiC was 98.5% SiC, 0.5% SiO_2, 0.3% Si, 0.08% Fe, 0.1% Al, 0.3% C.

The metal used was aluminium(170.1), the tensile strength of which was 65 MPa. Its composition was Al(99.77%), Fe(0.16%) and Si(0.07%) and the melting temperature was 660 °C.

The metal-matrix composites were fabricated by vacuum infiltration of a liquid metal into a porous preform under an argon pressure. The preform was a green body comprising SiC powder. During composite fabrication, the preform was placed at the bottom of a mould (Fig. 1), which was made of either low-carbon steel or graphite. In order to prevent direct contact between liquid aluminium and the steel mould, a layer (about 200 μm thick) of graphite powder was coated on the inner surface of the steel mould. The graphite layer deterred excessive reaction between aluminium and iron. Above the preform was placed a ceramic cloth layer and then an aluminium ingot. The ceramic cloth was used to prevent contact between the SiC preform and the aluminium melt before the infiltration pressure was applied. The mould chamber was evacuated using a mechanical pump (A0-A1 in Fig. 2). Then the chamber was heated to either 800 °C (for an infiltration temperature, T_p, of 780 ± 20 °C, A1-A2 in Fig. 2a) or 750 °C (for T_p of 700 or 670 °C, A1-A2 in Fig. 2b). The temperature was maintained for a period of time to ensure that the alloy

TABLE I Properties of SiC powder

Mean particle size	3.0 μm
Density	3.18 $g\,cm^{-3}$
Young's modulus	400–440 GPa
Thermal conductivity	90 $W\,m^{-1}\,K^{-1}$
Coefficient of thermal expansion	3.4 $\mu m\,m^{-1}\,°C^{-1}$
Crystal structure	Hexagonal

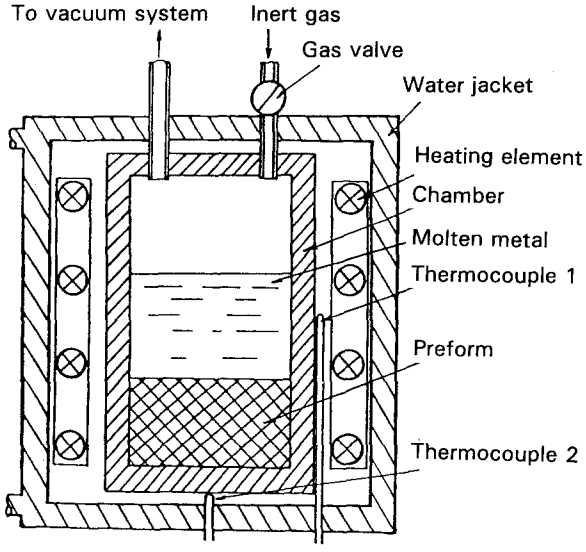

Figure 1 The apparatus for composite fabrication by vacuum infiltration of a liquid metal into a porous filler preform under an inert gas pressure.

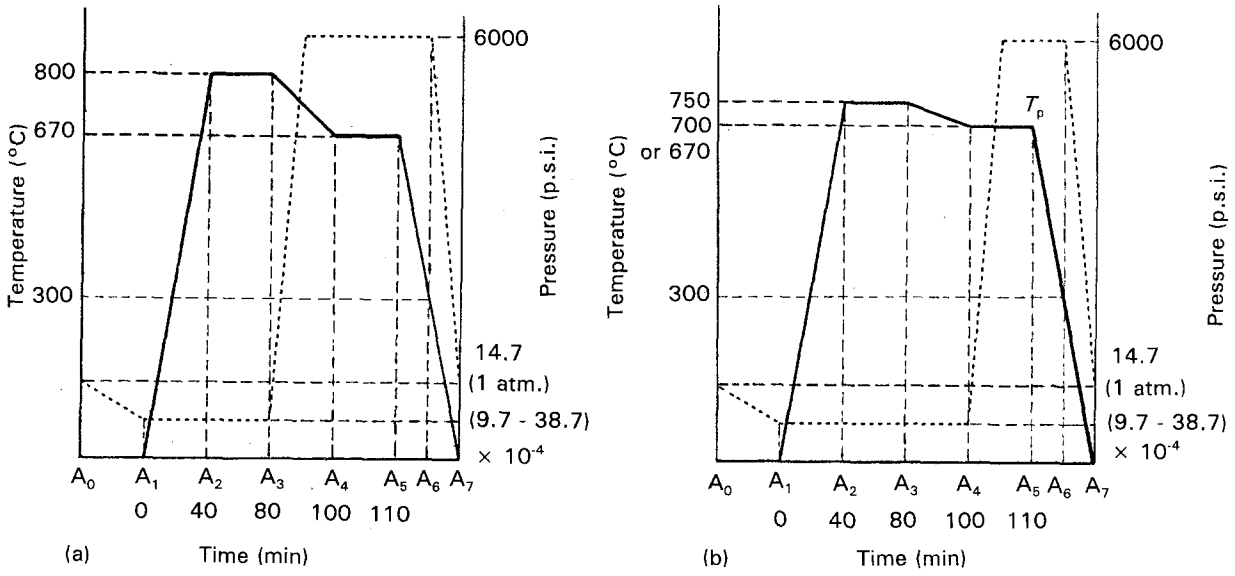

Figure 2 Variations in temperature and pressure during composite fabrication. (a) Infiltration temperatures of 780 ± 20 °C. (b) Infiltration temperatures of 700 and 670 °C.

melted completely and that the temperature of any part of the chamber was approximately equal (A2-A3 in Fig. 2). Then the temperature was allowed to drop at a rate of 3–10 °C min^{-1} to near the liquidus temperature, i.e. 670 °C (A3-A4 in Fig. 2a) or to the infiltration temperature, T_p, of 700 or 670 °C (A3-A4 in Fig. 2b). In order to study the effect of the infiltration temperature on the phase distributions and mechanical properties of the Al/SiC composites, three infiltration temperatures were used to fabricate the composites, namely 780 ± 20, 700 and 670 °C. In the case of T_p = 780 ± 20 °C, when the temperature just started to drop from 800 °C (A3-A4, in Fig. 2a), argon gas pressure started to be increased from 0 p.s.i. up to a maximum of 6000 p.s.i. (41 MPa). When the pressure reached 6000 p.s.i., the temperature dropped to 760 °C. In the case of T_p = 700 or 670 °C, the argon gas pressure started to be increased to 6000 p.s.i. when T_p was reached (A4-A5 in Fig. 2b). This pressure was applied to the surface of the melt to force the melt to penetrate the porous preform. Then the chamber was cooled with the help of a cooling water jacket outside the chamber (A5-A6 in Fig. 2). When the temperature was 300 °C, the pressure started to be released (A6-A7 in Fig. 2). For simplicity, notations of Al/SiC/780 °C/st, Al/SiC/700 °C/st and Al/SiC/670 °C/st are used to represent Al/SiC composites which were fabricated with a steel mould at T_p of 780 ± 20, 700 and 670 °C, respectively. Similarly, notations of Al/SiC/780 °C/gr, Al/SiC/700 °C/gr and Al/SiC/670 °C/gr represent Al/SiC composites which were fabricated with a graphite mould at T_p of 780 ± 20, 700 and 670 °C, respectively.

The SiC preforms were prepared by wet casting, which involved compressing in a die a slurry containing SiC powder, a liquid carrier (acetone) and a binder (a phosphate). The carrier/binder ratio was from 40:1 to 45:1 by volume, as this amount of binder was sufficient to maintain rigidity in the preform. Excessive amounts of binder caused the preform to be not porous enough for subsequent liquid-metal infiltration even at 6000 p.s.i. (41 MPa). The die allowed excessive liquid to be squeezed out. After removal from the die, the compact was dried in a fume hood at room temperature for 3 h. After drying, which removed most of the acetone, the preform was fired by (i) placing the preform in a furnace at room temperature, (ii) heating to 510 °C at a controlled rate of 1.4 °C min^{-1}, (iii) holding at 510 °C for 3 h, and (iv) cooling in the closed furnace. Excessive heating and a non-uniform temperature distribution in the furnace had to be avoided, as they would cause quick evolution of acetone and thermal stresses, thus resulting in cracking during the firing. The SiC preforms baked at 510 °C for 8 h gave the same X-ray diffraction peaks as the plain SiC powder. The preforms were cylinders, 4.00 cm diameter, with a height-to-diameter ratio of 0.3–0.5. In this paper, "composite cylinder" refers to the metal-infiltrated cylindrical preform; "excess aluminium" refers to the metal cast around the preform during infiltration.

The pressure used during compression of the slurry was adjusted to vary the SiC volume fraction in the resulting preform, although the range of volume fraction achieved was quite narrow. The SiC volume fraction was 55% and the height/diameter aspect ratio was 0.5 for all the composites used in this study.

2.2. Composite characterization

2.2.1. Metallography

Fig. 3 shows an optical micrograph of the centre-sectioned (i.e. the cross-section at the centre of the composite in a plane parallel to the cylindrical axis of the composite) Al/SiC which was fabricated with a steel mould at T_p of 670 °C. The bright regions in the photograph correspond to the excess aluminium cast around the composite. They occurred mainly at the top and side of the composite because infiltration took place from the top. An incompletely infiltrated portion

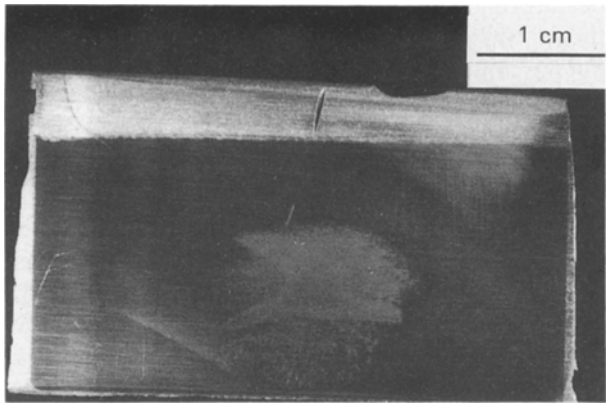

Figure 3 Optical micrograph of a polished vertical section of Al/SiC/670 °C/st, showing the portion of incomplete infiltration in the lower centre region of the composite cylinder.

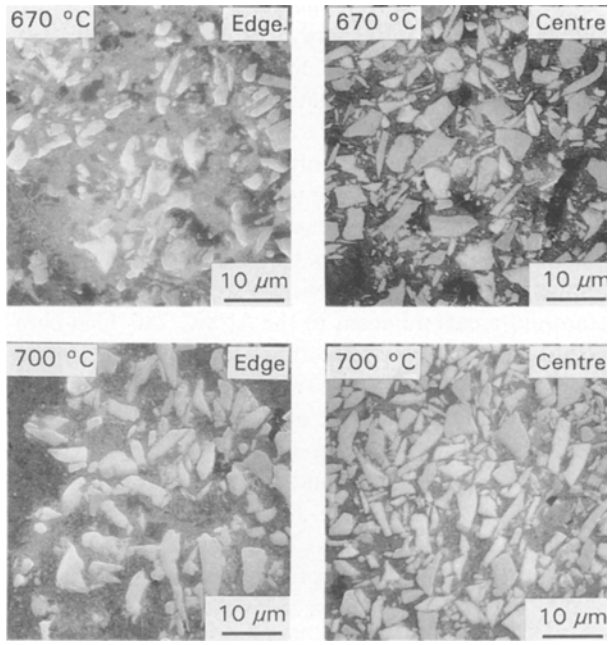

Figure 4 Scanning electron micrographs of polished sections of Al/SiC/700 °C/st and Al/SiC/670 °C/st in the edge and centre regions.

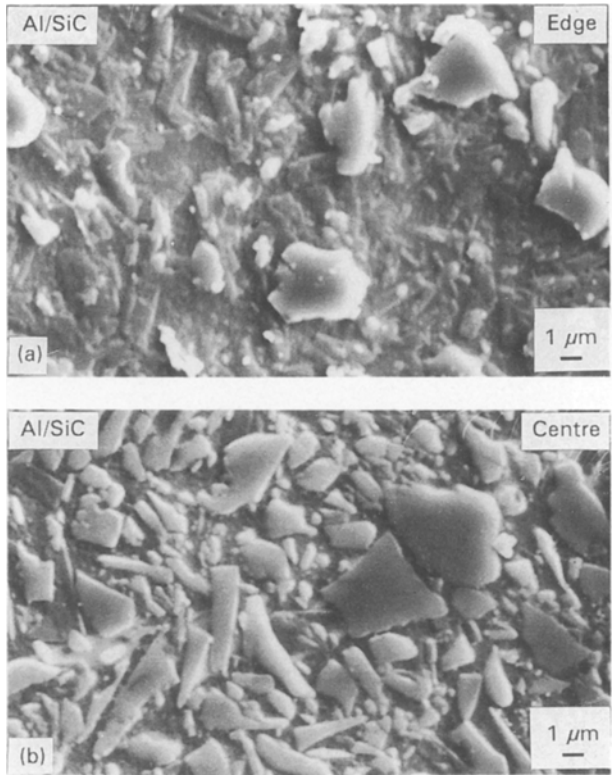

Figure 5 Scanning electron micrographs of a polished section of the Al/SiC/780 °C/st composite, showing the cylindrical edge and body centre regions of the composite cylinder.

was observed in the lower centre region of the composite cylinder. The infiltration temperature of 670 °C was not high enough for complete infiltration of liquid aluminium into the SiC preform. The aluminium melt solidified during the application of argon pressure so that not enough aluminium melt could be supplied to the lower centre region. The infiltration path was downwards and inwards from the top and the edge. The Al/SiC composite fabricated with a graphite mould at the same infiltration temperature of 670 °C showed a smaller incompletely infiltrated portion in the bottom centre region. No such phenomenon of incomplete infiltration was observed from composites fabricated with either steel or graphite moulds at 700 or 780 ± 20 °C.

Fig. 4 shows scanning electron micrographs (SEM) of the polished edge and centre regions of Al/SiC composite cylinders fabricated with a steel mould at T_p of 670 and 700 °C. Porosity was readily found in Al/SiC/670 °C/st, but little porosity was found in Al/SiC/700 °C/st. This indicates that the infiltration temperature of 670 °C was not high enough for sufficient infiltration before solidification. Increasing the infiltration temperature to 780 ± 20 °C further decreased the porosity, as shown in Fig. 5b for the centre of Al/SiC/780 °C/st. The porosity decreased with increasing infiltration temperature.

Although similar microstructures were observed in the centre and edge regions of Al/SiC/670 °C/st and Al/SiC/700 °C/st, different microstructures were found between the cylindrical edge and body centre regions of the Al/SiC/780 °C/st composite cylinder (Fig. 5). In Al/SiC/780 °C/st there were fewer SiC particles in the edge than the centre. The difference in microstructure, compared to those of Al/SiC/670 °C/st and Al/SiC/700 °C/st, is related to the more extensive interfacial reaction between aluminium and SiC in the edge region, which was next to the excess aluminium. More Al–SiC reaction occurred around the edge due to the proximity to the excess aluminium and a longer metal–particle contact time during infiltration. The reaction weakened the Al/SiC interface and consumed some SiC. The weakened interface probably caused some SiC particles to be partly removed during polishing. As compared to Fig. 6 of [13] (which shows a reaction product non-uniformly lining the Al/SiC interface after heating at 997 °C for 1 h), the clear-cut outlines of SiC particles in the centre region (Fig. 4) is an indication of relatively little reaction between aluminium and SiC at T_p of 670 or 700 °C.

Further evidence for the Al–SiC reaction is provided by SEM and energy dispersive spectroscopy (EDAX) observation of ternary Al–Fe–Si, binary Al–Fe and silicon precipitates in the excess aluminium cast around the composite cylinder. (This aluminium contained no preform). Only EDAX and morphology information of each phase was used to identify tentatively each phase. The X-ray diffraction peaks of these phases were too weak to be detected. Fig. 6 shows optical micrographs of polished sections of the excess aluminium cast adjacent to the Al/SiC/780 °C/st composite cylinder. Facetted ternary α-AlFeSi precipitates of about 100 μm in size were found in the excess aluminium lining the edge of the Al/SiC composite, as shown on the right in Fig. 6a. The ternary Al–Fe–Si precipitates were also found inside the edge region of the composite (left of Fig. 6a), but not in the central region of the composite. This indicates that iron-containing phases were present in the edge region of the composite (< 5 mm from the cylindrical edge) of Al/SiC/780 °C/st. Smaller needle-shaped silicon, Al_3Fe, Al_6Fe, β-AlFeSi and α-AlFeSi precipitates (tentative phase identification for phases other than silicon) were also present non-uniformly in the excess aluminium cast further away from the Al/SiC composite cylinder (Fig. 6b). The silicon was the product of the Al–SiC reaction; the iron-containing phases were due to contamination from the steel mould. The silicon was first formed in the edge region of the composite cylinder during infiltration and resulted in an Al–Si solution in the matrix. Because a difference in silicon concentration between the edge of the composite cylinder and the excess aluminium existed, the silicon tended to diffuse outward to the surrounding aluminium melt. The silicon diffusion continued until either the silicon concentrations in the composite cylinder and in the excessive aluminium were equalized, or the aluminium matrix solidified; the latter was

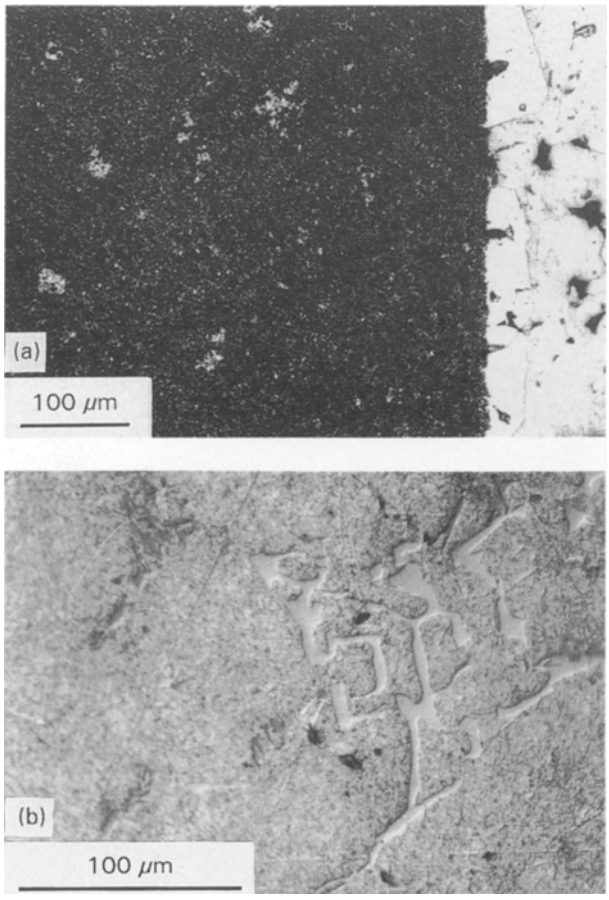

Figure 6 Optical micrographs of a polished section of the Al/SiC/780 °C/st composite, showing (a) facetted ternary Al–Fe–Si precipitates (bright) touching the edge of the composite (dark) and residing in the excess aluminium region (the right one-fifth of the photograph), (b) needle-shaped and smaller ternary Al–Fe–Si, binary Al–Fe and silicon precipitates in the excess aluminium region further away from the edge of the composite. (b) is at a higher magnification than (a).

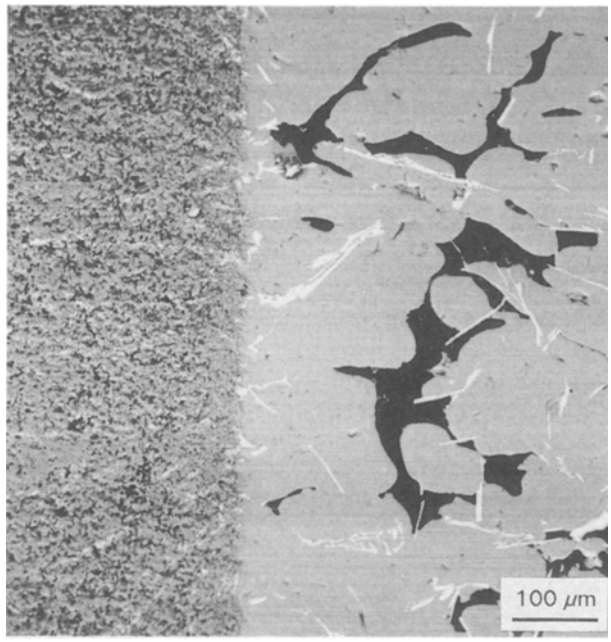

Figure 7 Optical micrograph of a polished section of Al/SiC/700 °C/st at the edge. The left 40% of the photograph is the composite itself; the right 60% of the photograph is the excess aluminium. Ternary Al–Fe–Si, binary Al–Fe and silicon precipitates were observed in the excess aluminium.

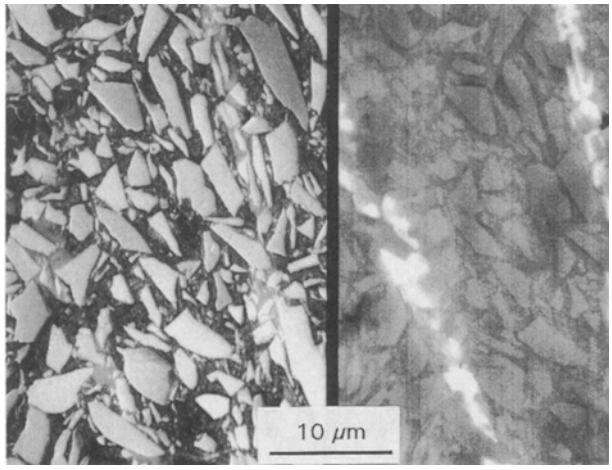

Figure 8 Scanning electron micrographs of a polished section in the edge of the Al/SiC/670 °C/st composite. The bright needle-shaped precipitate in the back-scattered electron image (right panel) was ternary Al–Fe–Si. The left panel is the secondary electron image of the same area as the right panel.

TABLE II Review of the crystallographic data of Al–Fe and Al–Fe–Si phases [11, 12, 14, 15]

Phase	Formula	Analytical composition (wt %)	Bravais lattice	Lattice parameters	References
θ	Al_3Fe $Al_{13}Fe_4$ $(Al,Si)_{13}Fe_4$		C-centred monoclinic C2/m	$a = 1.549$ nm $b = 0.808$ nm $c = 1.248$ nm $\beta = 107.75°$	[16–19]
	Al_mFe		Body-centred tetragonal	$a = 0.884$ nm $c = 2.160$ nm	[20]
	Al_9Fe_2		Monoclinic	$a = 0.890$ nm $b = 0.635$ nm $c = 0.632$ nm $\beta = 93.4°$	[21, 22]
	Al_6Fe		C-centred orthorhombic $Ccmm$	$a = 0.649$ nm $b = 0.744$ nm $c = 0.879$ nm	[23–26]
	Al_xFe		Unknown	Unknown	[27, 28]
α-AlFeSi	$Al_{12}Fe_3Si$		Body-centred cubic, $Im3$.	$a = 1.256$ nm 138 atoms/cell	[29]
α-AlFeSi	$Al_{20}Fe_5Si_2$	62.4 Al, 31.9 Fe, 5.6 Si	Body-centred cubic, $Im3$.	$a = 1.2548$ nm	[30]
α-AlFeSi	Al_8Fe_2Si		Primitive cubic, $Pm3$.	$a = 1.252$ nm	[31]
α′-AlFeSi	$Al_{12}Fe_3Si_2$	32.5 Fe, 8.4–10.3 Si	Hexagonal, $P6_3/mmc$	$a = 1.230$ nm $c = 2.620$ nm	[32]
α″-AlFeSi q_1-AlFeSi			C-centred orthorhombic	$a = 1.270$ nm $b = 3.620$ nm $c = 1.270$ nm	[27, 33]
α_T-AlFeSi			C-centred monoclinic	$a = 2.795$ nm $b = 3.062$ nm $c = 2.073$ nm $\beta = 97.74°$	[34]
q_2-AlFeSi			Monoclinic	$a = 1.250$ nm $b = 1.230$ nm $c = 1.970$ nm $\beta = 111.0°$	[33]
β-AlFeSi	$Al_9Fe_2Si_2$	58.2–59.3 Al, 26.9–27.4 Fe, 13.5–15.2 Si	Monoclinic	$a = 0.612$ nm $b = 0.612$ nm $c = 4.150$ nm $\beta = 91.0°$	[30, 35]
β*-AlFeSi			Monoclinic	$a = 0.890$ nm $b = 0.490$ nm $c = 4.160$ nm $\beta = 92.0°$	[27]
γ-AlFeSi	Al_3FeSi	33–38 Fe, 13–18.5 Si	C-centred monoclinic	$a = 1.780$ nm $b = 1.025$ nm $c = 0.890$ nm $\beta = 132.0°$	[36]
δ-AlFeSi	Al_4FeSi_2	47.08 Al, 27.04 Fe, 25.01 Si	Tetragonal	$a = 0.614$ nm $c = 0.948$ nm	[30, 37]
δ-AlFeSi	Al_3FeSi_2		Tetragonal	$a = 0.607$ nm $c = 0.950$ nm	[38]
α-Si	Si		Diamond, cubic $Fd3m$	$a = 0.543$ nm	[39]

Notes:
1. α-AlFeSi phases usually appear as curved lines when formed eutectically, especially when the silicon content is not low. They may also form polyhedrons, irregular shapes or Widmanstatten-type precipitates.
2. β-AlFeSi phases are flaky when formed eutectically. In section they appear as needles.
3. δ-AlFeSi phases appear in the form of platelets.
4. The Al_3Fe phase appears as elongated flakes or star-shaped clusters when eutectically formed. It resists coalescence.
5. The Al_6Fe phase appears as a metastable phase at a high solidification rate. It forms a fine lamellar eutectic. As a primary or coarse eutectic, it forms solid or hollow parallelograms.

more likely. Thus, a non-uniform silicon distribution throughout the composite cylinder resulted.

The α-AlFeSi, β-AlFeSi, Al_3Fe, Al_6Fe and silicon precipitates (tentative phase identification for phases other than silicon) were also observed in the excess aluminium cast around Al/SiC/700 °C/st. As shown in Fig. 7, the Al/SiC/700 °C/st composite also exhibited facetted Al–Si–Fe precipitates (smaller than those in Al/SiC/780 °C/st, Fig. 6a) lining the edge of the Al/SiC composite in the excess aluminium side (on the right in Fig. 7) and needle-shaped ternary Al–Si–Fe, binary Al–Fe and silicon precipitates elsewhere in the excess aluminium. However, only ternary Al–Si–Fe and binary Al–Fe (with no or little silicon) precipitates were found in the excess aluminium associated with Al/SiC/670 °C/st (micrograph not shown). This indicates that the Al–SiC reaction occurred even at $T_p = 670$ °C, though the reaction was less severe for Al/SiC fabricated at 670 °C. Fig. 8 shows a scanning electron micrograph of the edge region of the Al/SiC/670 °C/st composite cylinder. The bright needle-shaped precipitates in the back-scattered scanning electron micrograph (on the right in Fig. 8) were identified by EDAX as a ternary Al–Fe–Si phase. Table II gives a summary review of the crystallographic data of various Al–Fe and Al–Fe–Si phases. Although phase identification was only tentatively made in this work, that the observed phases included Al–Fe and Al–Fe–Si for the case of a steel mould, was clear.

Only the silicon precipitate was observed in the excess aluminium surrounding the Al/SiC composite cylinders fabricated with a graphite mould at 780 ± 20, 700 and 670 °C. The amount of silicon in the excess aluminium increased with increasing infiltration temperature. Fig. 9 shows an optical micrograph of Al/SiC/780 °C/gr, in which silicon in the form of eutectic Al–Si was readily observed between the primary aluminium dendrites. This indicates that silicon, a product of the Al–SiC reaction, diffused outward to the excess aluminium and formed a hypoeutectic Al–Si alloy.

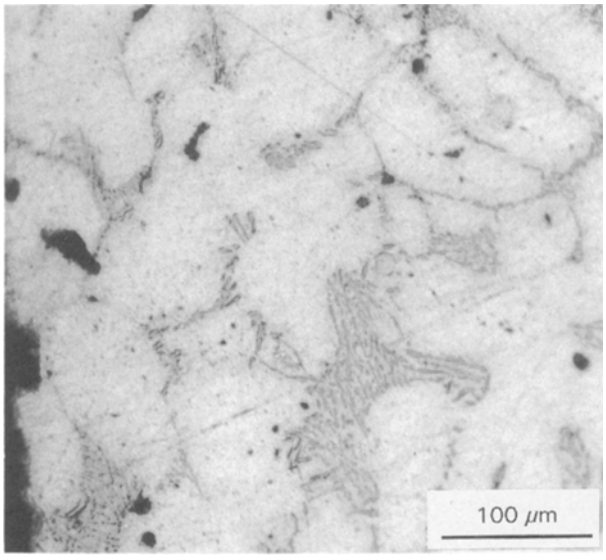

Figure 9 Optical micrograph of a polished section in the edge of the Al/SiC/780 °C/gr composite. Only silicon precipitates in the form of Al–Si eutectic were found between the dendrites.

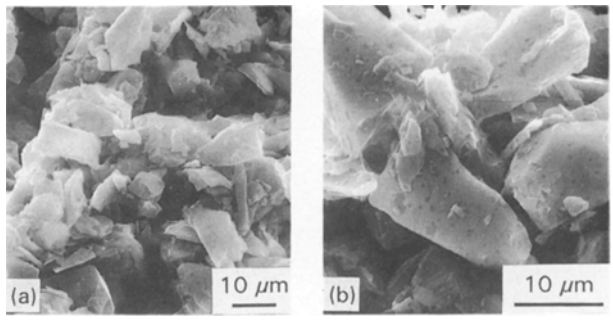

Figure 10 Scanning electron micrographs of a fully etched Al/SiC/700 °C/gr composite. Silicon precipitated and bridged adjacent SiC particles. (b) is at a higher magnification than (a).

No Al–Si eutectic or dendritic morphology was microscopically observed within the Al/SiC composite cylinders fabricated with either steel or graphite moulds at all infiltration temperatures. This negative observation may be due to the very small SiC particle spacing in the Al/SiC composite. In order to study the location of silicon in Al/SiC, Al/SiC/700 °C/gr was etched with acids to remove completely the aluminium. Unlike the preform which showed clean isolated SiC particles (not shown), Fig. 10a shows that the SiC particles were connected to form a network. Fig. 10b is a scanning electron micrograph at a higher magnification, which shows that silicon precipitated between adjacent SiC particles, thereby forming a network.

2.2.2. X-ray diffraction

X-ray diffraction (XRD) was performed with CuK_α radiation in different regions of the Al/SiC composite cylinder in order to investigate the phase distribution. For the Al/SiC/780 °C/st composite, the matrix throughout the composite contained crystalline silicon with a non-uniform distribution, as the silicon peak intensities varied from spot to spot in the composite. Weak Al_4C_3 peaks were also observed. The low intensity of the Al_4C_3 peaks was partly due to the fact that Al_4C_3 was unstable in moisture and tended to be etched away during sample preparation. Selected regions of the composite were locally ground into powder (by filing) for powder X-ray diffraction. These regions were (i) the region (labelled "edge") at the cylindrical edge of the composite halfway up the cylinder, within 1.2 mm from the halfway point (vertically) and within 1.5 mm from the cylindrical edge along the radius (horizontally), (ii) the body centre of the composite cylinder (labelled "centre"), within 1.2 mm from the centre along the cylindrical axis (vertically) and within 1.0 mm from the centre along the radius (horizontally), (iii) the top of the composite cylinder (labelled "top"), within 1.0 mm from the halfway point along a radius (horizontally) and within 2.5 mm from the top face of the cylinder (vertically), and (iv) the bottom of the composite cylinder (labelled "bottom"), within 1.0 mm from the halfway point along a radius (horizontally) and within 2.5 mm from the bottom face

of the cylinder (vertically). Fig. 11 shows the diffraction patterns of the "edge" and "centre" only. The ratio of the integrated intensity of the strongest SiC peak to that of the Al(2 0 0) peak was 1.10, 1.18, 1.56 and 1.63 for the "top", "edge", "bottom" and "centre", respectively. This means that the consumption of SiC due to the reaction with aluminium was non-uniform, such that the consumption was more severe in the "top" and "edge", which were next to the interface with the excess aluminium, than in the "bottom" and "centre", which were far away from this interface. This observation is consistent with the scanning electron micrographs of Fig. 5, which shows fewer SiC particles in the edge than the centre. Similarly, the Al_4C_3 peaks (though weak) were stronger in the "top" and "edge" than in the "bottom" and "centre".

Fig. 12 shows the XRD patterns of the excess aluminium and the "edge" of the Al/SiC/780 °C/gr composite cylinder, which was similarly prepared as Al/SiC/780 °C/st. Only aluminium and silicon peaks were present in the excess aluminium surrounding the composite cylinder. No Al_4C_3 peak was found in the excess aluminium, even though this region was next to the graphite mould. However, in the "edge" of composite cylinder, Al_4C_3 peaks were weakly present, due to the reaction between SiC and aluminium. This is consistent with the XRD results of Al/SiC/780 °C/st.

The silicon peaks in Fig. 11 are very weak, so the silicon distribution could not be investigated in the same way as the SiC or Al_4C_3 distributions. In order to investigate the silicon distribution, powder X-ray diffraction of the composite was performed separately on powder samples obtained by scraping off from different regions of the acid-etched composite cylinder. The acid solution contained HCl, H_2SO_4 and water in the ratio 1:1:5. The solution etched away aluminium and Al_4C_3, but not silicon or SiC. After aluminium and Al_4C_3 had been completely etched away, the specimens were successively rinsed with distilled water, acetone and alcohol, and then dried in a vacuum dryer at < 100 °C.

Fig. 13 shows an X-ray diffraction pattern of the etched Al/SiC/780 °C/st composite for the region in the centre of the bottom face of the composite cylinder (within 1.0 mm from the centre along a radius and within 2.5 mm from the bottom face). X-ray diffraction patterns (not shown) were also taken for the region in the body centre of the composite cylinder (within 1.2 mm from the centre along the cylindrical axis and within 10 mm from the centre along the radius) and the region in the centre of the top face of the composite cylinder (within 1.0 mm from the centre along a radius and within 2.5 mm from the top face). Silicon peaks were observed in all three regions of the etched composite, indicating that SiC reacted with aluminium throughout the whole composite cylinder. The Si/SiC integrated intensity ratio of the most dominant silicon and SiC peaks in each of three circular slices (namely, top, middle and bottom slices) of the composite cylinder is shown in Fig. 14 as a function of the distance along a radius from the cylindrical edge to the centre of the composite cylinder. The thickness of each slice was 2.5 mm. The intensity ratio increased with increasing distance from the edge of the composite cylin-

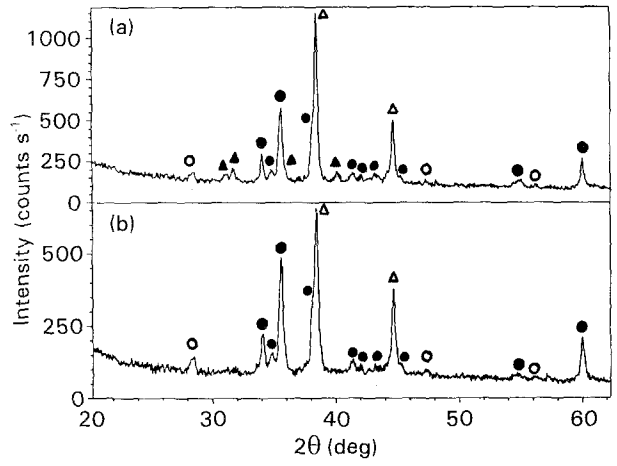

Figure 11 Powder X-ray diffraction patterns of the edge and centre regions of the Al/SiC/780 °C/st composite cylinder. (a) Edge, (b) centre. (●) SiC, (○) Si, (▲) Al_4C_3, (△) Al.

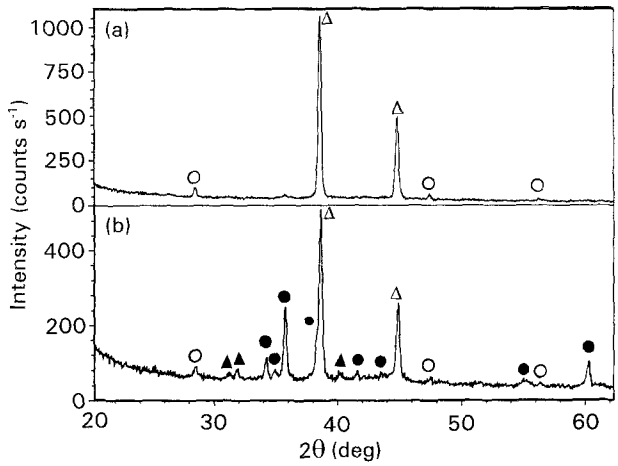

Figure 12 Powder X-ray diffraction patterns of the excess aluminium and the edge regions of Al/SiC/780 °C/gr composite cylinder. (a) Excess aluminium surrounding the composite cylinder, (b) edge. (●) SiC, (○) Si, (▲) Al_4C_3, (△) Al.

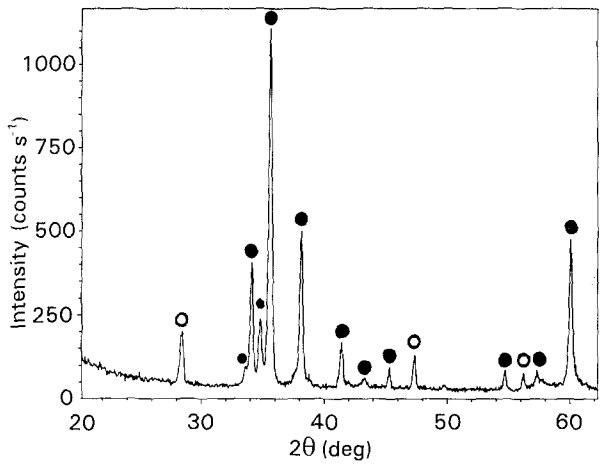

Figure 13 Powder X-ray diffraction pattern of the Al/SiC/780 °C/st composite with aluminium and Al_4C_3 removed by etching. The pattern was taken from the centre of the bottom face of the composite cylinder. (●) SiC, (○) Si.

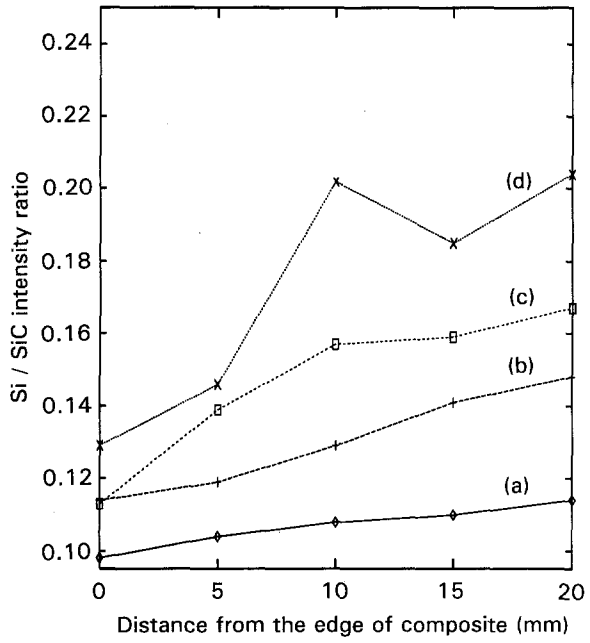

Figure 14 The Si/SiC integrated intensity ratio (from X-ray diffraction) as a function of the distance from the cylindrical edge of the Al/SiC/780 °C/st composite cylinder. (a) Top slice of cylinder, (b) middle slice, (c) bottom slice, and (d) middle slice after heating the composite at 600 °C for 480 h.

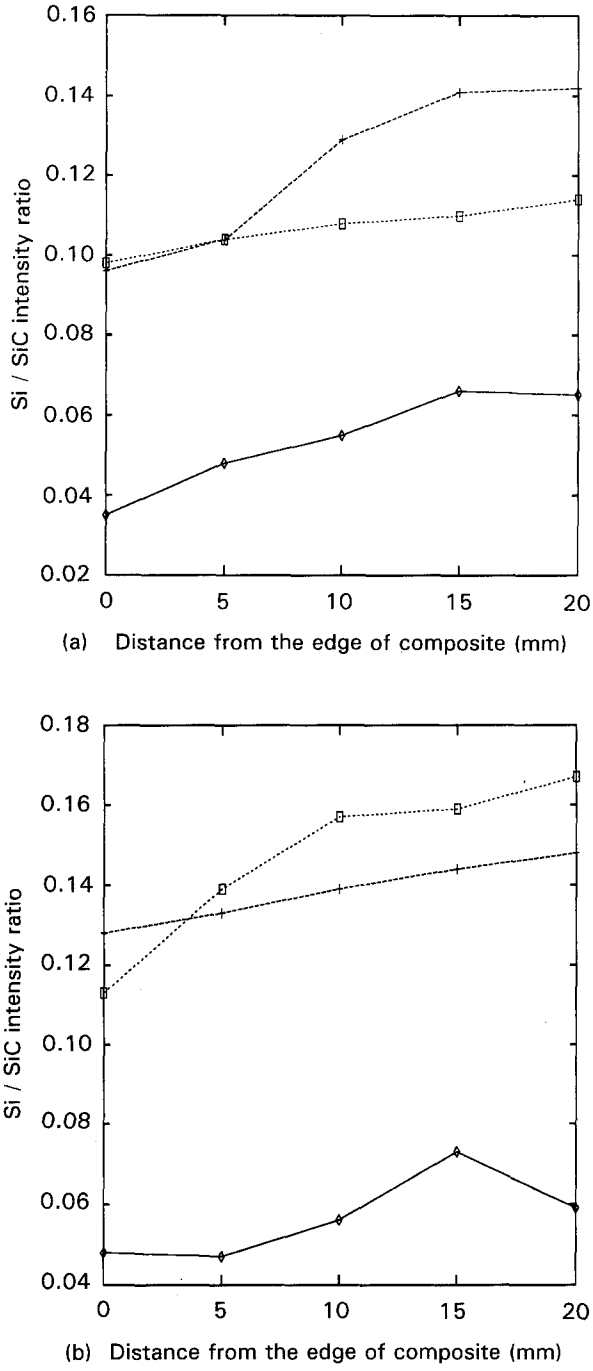

Figure 15 The Si/SiC integrated intensity ratio (from X-ray diffraction) as a function of the distance from the cylindrical edge of the Al/SiC composite cylinders fabricated with a steel mould at various infiltration temperatures. (a) The top slice of each composite, (b) the bottom slice of each composite. (◇) 670 °C, (+) 700 °C, (□) 780 °C.

der for each slice. Its value was lowest in the top region and highest in the bottom region. This indicates that, after complete infiltration of aluminium into the SiC preform, the reaction between liquid aluminium and SiC continued. The silicon formed diffused from the composite cylinder upward and outward into the aluminium melt surrounding the composite, because excess aluminium melt existed above and around the composite and negligibly below the composite. The least amount of silicon diffusion is expected from the centre of the bottom region, as this point is furthest from the interface between the composite and the aluminium melt. Thus, the Si/SiC ratio at the centre of the bottom slice was most representative of the amount of Al–SiC reaction for each infiltration temperature.

Fig. 14 also shows that the Si/SiC ratio of Al/SiC/780 °C/st in the middle slice of the composite cylinder increased significantly after heat treatment of the composite (with the excess aluminium removed before the heat treatment) in air at 600 °C for 480 h. This indicates that the reaction of SiC with the silicon-containing aluminium alloy continued at 600 °C, although it was suggested that a silicon-containing aluminium alloy prevented the reaction of SiC with aluminium during casting [6].

In order to study the silicon distributions in the Al/SiC composites fabricated at 670 and 700 °C, powder X-ray diffraction was performed for the etched Al/SiC/700 °C/st composite and the etched Al/SiC/670 °C/st composite, which were prepared by using the same etching procedure as the etched Al/SiC/780 °C/st composite of Fig. 14. Fig. 15 shows the Si/SiC intensity ratio in the top (a) and bottom (b) slices of Al/SiC fabricated at each of the three infiltration temperatures. Both top and bottom slices of each composite show a trend of increasing Si/SiC ratio as the distance from the edge of the composite cylinder increased. For both the top and bottom slices, the Si/SiC intensity ratio was higher for T_p = 780 and 700 °C than 670 °C. For T_p = 780 °C, the variation of the Si/SiC intensity ratio was larger in the bottom slice than the top slice. This is because of (i) the severity of the SiC–Al reaction at 780 °C, and (ii) the fact that the whole of the top slice was in contact with liquid aluminium from the start of infiltration, whereas different parts of the bottom slice were in contact with liquid aluminium for different lengths of time. For T_p = 780 °C, the Si/SiC intensity ratio was higher in the bottom slice than the

top slice. This is because of more extensive out-diffusion of silicon from the top slice, which was adjacent to the excess liquid aluminium, than the bottom slice. For each of the infiltration temperatures of 700 and 670 °C, the Si/SiC intensity ratio was similar in the bottom and top slices.

X-ray diffraction was similarly used to measure the Si/SiC intensity ratio variation in Al/SiC fabricated with a graphite mould at various infiltration temperatures. Fig. 16 shows this ratio of Al/SiC/780 °C/gr as a function of the distance along a radius from the cylindrical edge of the top, middle and bottom slices. As also observed in composites made with a steel mould at 780 °C (Fig. 14), the lowest Si/SiC ratio occurred in the top slice and the highest ratio occurred in the bottom slice (Fig. 16). Al/SiC/780 °C/gr (Fig. 16) exhibited larger values of the Si/SiC intensity ratio at all corresponding positions than Al/SiC/780 °C/st (Fig. 14). Higher values of the Si/SiC intensity ratio were also found in Al/SiC/700 °C/gr and Al/SiC/670 °C/gr, compared to those of Al/SiC/700 °C/st and Al/SiC/670 °C/st, respectively. This means that more Al–SiC reaction occurred in composites fabricated with a graphite mould than those fabricated with a steel mould. This may be due to a longer contact time between liquid aluminium and SiC in composites fabricated with a graphite mould, because the graphite mould had a lower thermal conductivity than a steel mould and thus caused the composite to cool more slowly. Furthermore, the difference in the Si/SiC intensity ratio between the top and middle slices of Al/SiC/780 °C/gr (Fig. 16) was larger than that in Al/SiC/780 °C/st (Fig. 14). This indicates that there was a longer time for silicon to diffuse outwards and upwards into the excess liquid aluminium before solidification for Al/SiC/780 °C/gr than Al/SiC/780 °C/st.

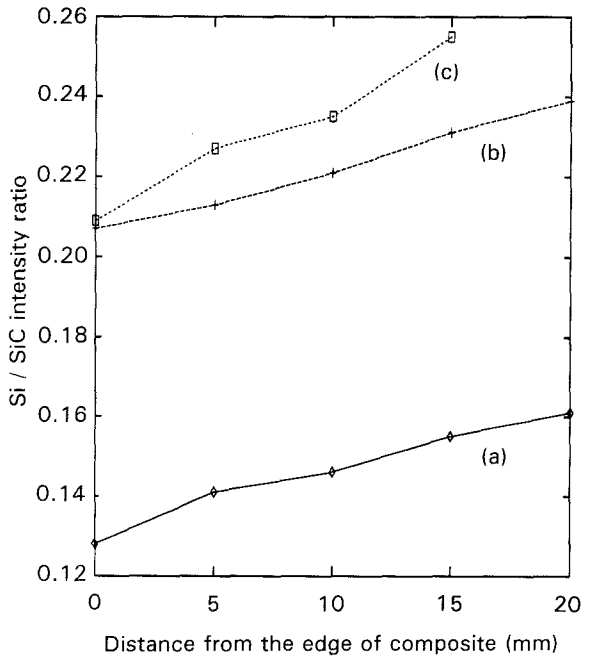

Figure 16 The Si/SiC integrated intensity ratio (from X-ray diffraction) as a function of the distance from the cylindrical edge of the Al/SiC/780 °C/gr composite cylinder. (a) Top slice of the cylinder, (b) middle slice, (c) bottom slice.

Fig. 17 shows the Si/SiC intensity ratio in the top (Fig. 17a) and bottom (Fig. 17b) slices of Al/SiC fabricated with a graphite mould at each of the three infiltration temperatures. Both slices show a trend of increasing Si/SiC ratios as the distance from the edge of the composite cylinder increased. The ratio increased with increasing infiltration temperature for each of the top and bottom slices. In contrast to the case of a steel mould, for which the Si/SiC ratio was quite similar for infiltration temperatures of 780 and 700 °C (Fig. 15), the Si/SiC ratio was larger at 780 than 700 °C when a graphite mould was used (Fig. 17). These characteristics of the composites fabricated with

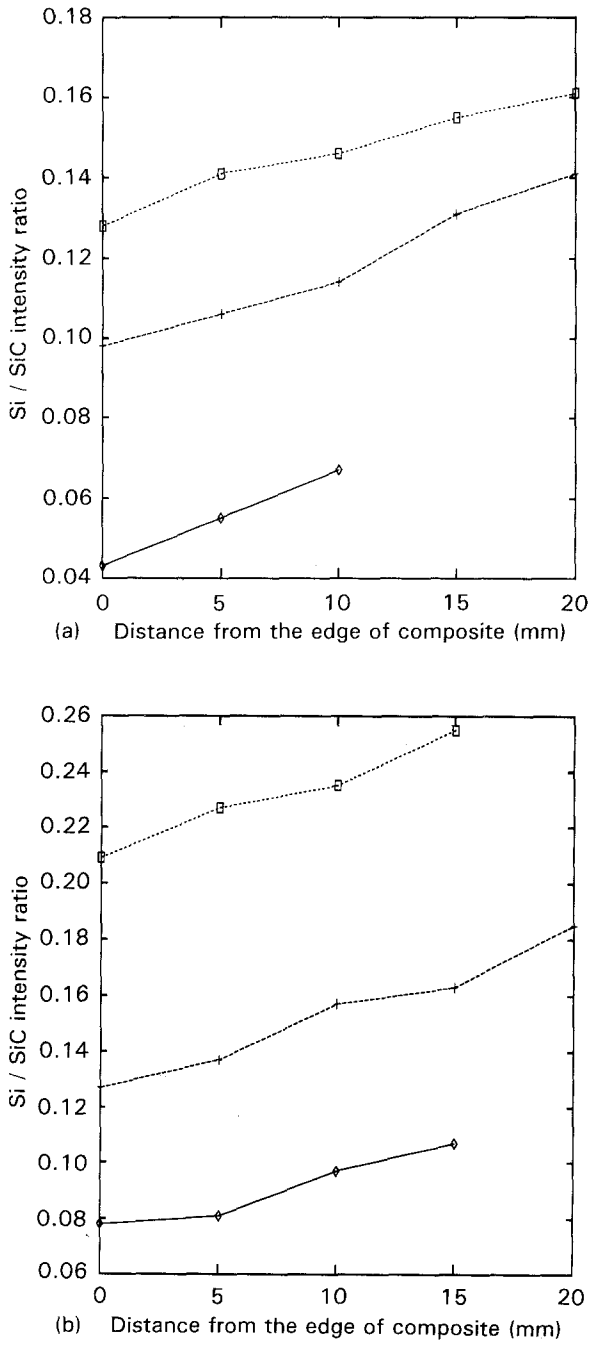

Figure 17 The Si/SiC integrated intensity ratio (from X-ray diffraction) as a function of the distance from the cylindrical edges of the Al/SiC composite cylinders fabricated with a graphite mould at various infiltration temperatures. (a) The top slice of each composite, (b) the bottom slice of each composite. (◇) 670 °C, (+) 700 °C, (□) 780 °C.

a graphite mould are due to the longer silicon out-diffusion time for a graphite mould than a steel mould.

In order to investigate the actual silicon content in the matrix of Al/SiC, two kinds of silicon powders were mixed with the SiC powder at various atomic Si/SiC ratios for X-ray diffraction. One kind of silicon was amorphous silicon powder (Sicomill UN1346) which was obtained from KemaNord Industrikemi. Although it was rated amorphous, clear silicon X-ray diffraction peaks were found. The other kind of silicon powder was obtained by grinding a 99.9999% pure polycrystalline silicon lump, which was obtained from Fisher Scientific Co. Fig. 18 shows that both Si/SiC mixtures gave a linear relationship between the Si/SiC X-ray intensity ratio thus obtained and the atomic Si/SiC atomic ratio was 2.2795, which was obtained by the least squares method. Table III shows the silicon content (at %) in the matrix of Al/SiC (55 vol % SiC, bottom section), as obtained from X-ray diffraction results and the conversion provided by Fig. 18. The silicon content in the matrix of Al/SiC increased with increasing distance from the edge of the composite cylinder, whether steel or graphite moulds were used. The silicon content tended to increase with increasing temperature for the same mould material. It tended to be higher for the graphite mould than the steel mould for the same infiltration temperature. The highest silicon content of 9.93 at % was observed in the centre (20 mm from the edge) of the composite fabricated at 780 °C with the graphite mould. Even this highest silicon content was below the silicon content of the Al–Si eutectic.

Because various values of the Si/SiC intensity ratio existed throughout the composite cylinder, the Si/SiC intensity ratio at the centre of the bottom slice was used to investigate the effect of the infiltration temperature on the extent of the Al–SiC reaction. Fig. 19 shows the effect of the infiltration temperature, T_p, on the silicon content at the centre of the bottom slice for each of the composites made with steel and graphite moulds. At each infiltration temperature, the silicon content was higher for the composite fabricated with the graphite mould than that fabricated with the steel mould. The silicon content in the matrix indicates the extent of the Al–SiC reaction; it increased abruptly from T_p of 670 °C to T_p of 700 °C, but increased gradually from T_p of 700 °C to T_p of 780 ± 20 °C.

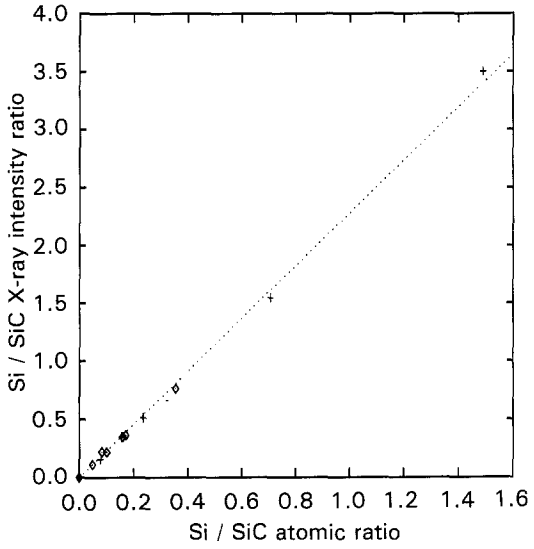

Figure 18 The linear relationship of the Si/SiC X-ray intensity ratio and the Si/SiC atomic ratio. (◇) Silicon powder A, (+) silicon powder B.

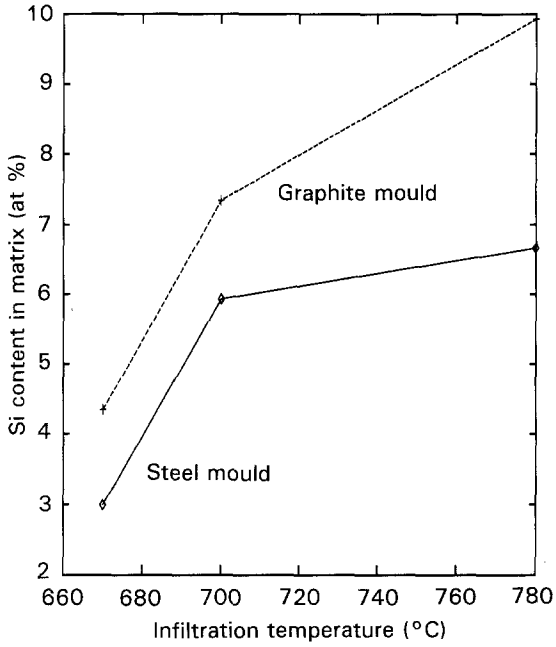

Figure 19 The silicon content (at %, obtained from X-ray spectroscopy) in the matrix of Al/SiC composites as a function of the infiltration temperature.

TABLE III The silicon content in the aluminium matrix of Al/SiC (55 vol % SiC, bottom section) fabricated with steel and graphite moulds at various infiltration temperatures. The results were obtained from X-ray diffraction

Mould	Infiltration temperature (°C)	Silicon content (at %) at distance from the edge of the composite cylinder				
		0 mm	5 mm	10 mm	15 mm	20 mm
Steel	670	1.98	1.94	2.31	2.99	
Graphite	670	3.19	3.31	3.94	4.34	
Steel	700	5.12	5.19	5.28	5.78	5.93
Graphite	700	5.12	5.51	6.28	6.51	7.34
Steel	780 ± 20	4.58	5.59	6.28	6.36	6.66
Graphite	780 ± 20		8.24	8.91	9.20	9.93

The Al–SiC reaction rate is expected to decrease with increasing extent of infiltration, as the aluminium matrix contains more silicon as infiltration proceeds, thereby causing further Al–SiC reaction to diminish [6].

2.2.3. Differential scanning calorimetry

A Perkin–Elmer differential scanning calorimeter (DSC 7) was used to measure the melting temperatures and associated enthalpy changes of the phases or microconstituents in the matrix of the Al/SiC composite and in the excess aluminium around the composite cylinder.

Fig. 20 shows DSC thermograms of the Al/SiC/780 °C/st composite, obtained on cooling from 700 °C to 500 °C at a cooling rate of 10 °C min^{-1}, for three local regions in the bottom slice (1 mm thick) of the composite cylinder. The three local regions were A (the edge of the slice, within 1 mm from the cylindrical edge, such that the region was within the composite), B (the centre of the slice, within 0.5 mm from the centre) and C (the excess aluminium adjacent to the edge of the composite, within 1 mm from the edge). Region A exhibited exothermic peaks with onsets at 574, 607 (not very clear) and 622 °C; Region B exhibited exothermic peaks with onsets at 573 and 608 °C; Region C exhibited exothermic peaks with onsets at 573, 593 and 624 °C. All peaks were reversibly observed upon the first heating and subsequent heating and cooling. The first peak for each region, i.e. the one at 573–574 °C, is attributed to the Al–Si eutectic melting (the solidus) at 577 °C. The second peak for each region, at 622 °C for Region A, 608 °C for Region B or 624 °C for Region C, is attributed to the liquidus of the Al–Si alloy matrix. The third peak, which was only observed in Region A (607 °C) and Region C (608 °C), is associated with one or more of the following invariant reactions in the Al–Fe–Si system [14]:

$$L(93\text{ wt \% Al, }2\text{ wt \% Fe, }3\text{ wt \% Si}) + FeAl_3 \rightleftharpoons Al + \alpha\text{-AlFeSi} \quad \text{at } 620\,^{\circ}C$$

$$L(93\text{ wt \% Al, }2\text{ wt \% Fe, }5\text{ wt \% Si}) + \beta\text{-AlFeSi} \rightleftharpoons Al + \alpha\text{-AlFeSi} \quad \text{at } 615\,^{\circ}C$$

$$L(85\text{ wt \% Al, }1\text{ wt \% Fe, }14\text{ wt \% Si}) + \delta\text{-AlFeSi} \rightleftharpoons Si + \alpha\text{-AlFeSi} \quad \text{at } 600\,^{\circ}C$$

The crystallographic data and compositions of various ternary Al–Si–Fe solid phases are shown in Table II.

The invariant reaction at 600 °C did not apply because the third peak onset on cooling was above 600 °C and the invariant reaction of forming δ-AlFeSi was around 790 °C for an aluminium melt containing 21% Si and 18% Fe [14, 15]. Furthermore, the results from X-ray diffraction showed that the matrix in the Al/SiC composite was hypoeutectic Al–Si, while the aluminium melt for the invariant reaction at 600 °C was hypereutectic Al–Si containing 14 wt % Si and 1 wt % Fe. Metallurgical examination suggested that both α-AlFeSi and β-AlFeSi were present in the excess

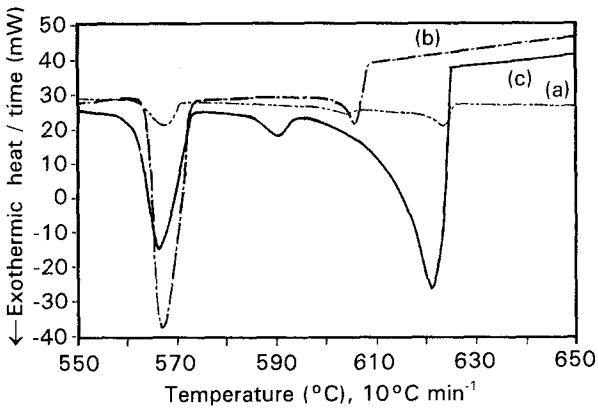

Figure 20 DSC scans showing exothermic peaks upon cooling. (a) The centre of the middle slice of the composite cylinder, (b) the edge of the slice within the composite, (c) the excess aluminium adjacent to the edge of the Al/SiC/700 °C/st composite.

aluminium. Thus, the third peak was attributed to the Al–α-AlFeSi eutectic melting [6, 14, 15]. The presence of iron in Regions A and C was confirmed by energy-dispersive X-ray spectroscopy. However, X-ray spectroscopy of Region B showed no peak other than those of aluminium and silicon. The absence of the third DSC peak in Region B indicates no iron contamination from the mould in this region. In all regions, no other peak was observed up to 700 °C; the absence of a peak at 660 °C indicates the absence of pure aluminium in all regions, even though pure aluminium was used for infiltration.

DSC was performed for composites fabricated with a steel mould at all three infiltration temperatures, i.e. 780, 700 (Fig. 20) and 670 °C. Only the solidus (eutectic) and liquidus of the Al–Si melting were observed at the centre of composites fabricated at all three infiltration temperatures. This indicates that there was no iron contamination at the centre of all composites and that the Al–SiC reaction occurred even at the lowest infiltration temperature of 670 °C. Other than the solidus and liquidus of Al–Si, an additional invariant reaction associated with ternary Al–Si–Fe was observed in the temperature range from 600–620 °C for both the excess aluminium and the edge region (< 2 mm from the cylindrical edge) of the composite fabricated at 700 °C and only the edge region of the composite fabricated at 670 °C. This additional DSC peak attributed to the Al–α-AlFeSi eutectic melting, as in the case of infiltration at 780 °C. For the excess aluminium associated with the composite fabricated at 670 °C, only the invariant reaction due to the Al–Fe melting was observed in addition to the solidus and liquidus of Al–Si.

The temperature difference, ΔT, between the first peak (corresponding to solidus or the eutectic temperature) and the second peak (corresponding to the liquidus) was used to evaluate the silicon content in each region of a composite. The ΔT values were 35, 48 and 51 °C for Regions B, A and C, respectively, of the composite fabricated with a steel mould at 700 °C (Fig. 20). As shown in Tables IV and V for composites fabricated with steel and graphite moulds, respectively, ΔT decreased with increasing distance from the

TABLE IV The liquidus–solidus temperature difference, ΔT, and silicon content in the aluminum matrix of Al/SiC (55 vol % SiC, bottom section) fabricated with a steel mould at various infiltration temperatures. The results were obtained from DSC

Infiltration temperature (°C)		Distance from the edge of the composite cylinder				
		0 mm	5 mm	10 mm	15 mm	20 mm
670	ΔT(°C)	63.55	60.51	55.22	[a]	[a]
	Si (at %)	2.81	3.26	4.03	[a]	[a]
700	ΔT(°C)	54.04	50.55	48.14	45.39	40.25
	Si (at %)	4.20	4.71	5.06	5.47	6.22
780 ± 20	ΔT(°C)	46.69	44.07	40.76	37.26	34.21
	Si (at %)	5.28	5.66	6.14	6.65	7.10

[a] Region of incomplete infiltration.

TABLE V The liquidus–solidus temperature difference, ΔT, and silicon content in the aluminum matrix of Al/SiC (55 vol % SiC, bottom section) fabricated with a graphite mould at various infiltration temperatures. The results were obtained from DSC

Infiltration temperature (°C)		Distance from the edge of the composite cylinder				
		0 mm	5 mm	10 mm	15 mm	20 mm
670	ΔT(°C)	59.49	55.22	54.82	[a]	[a]
	Si (at %)	3.41	4.03	4.09	[a]	[a]
700	ΔT(°C)	50.99	47.20	40.04	32.52	28.28
	Si (at %)	4.65	5.20	6.25	7.35	7.97
780 ± 20	ΔT(°C)	37.73	34.77	31.21	24.42	21.36
	Si (at %)	6.59	7.02	7.54	8.53	8.98

[a] Incomplete infiltration region.

edge to the centre of the composite cylinder, and decreased with increasing infiltration temperature. This means that the silicon content increased with increasing infiltration temperature and increased with increasing distance from the edge to the centre, as can be seen by referring to the Al–Si phase diagram (Fig. 21). Furthermore, the silicon content was lower in Region C than Region A. Comparison of Tables IV and V shows that the silicon content was higher in the composite fabricated with the graphite mould than that fabricated with the steel mould at each corresponding location in the composite cylinder.

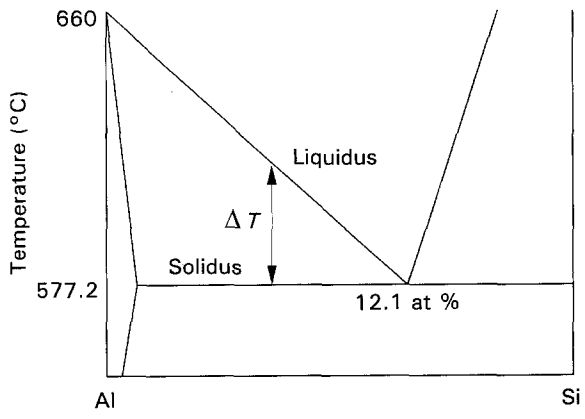

Figure 21 The Al–Si phase diagram (not to scale) used for the determination of the silicon content (at %) in the matrix of Al/SiC composites. As the liquidus–solidus temperature difference, ΔT, decreases, the silicon content, X, in the aluminium matrix increased; $X = (12.1)(1 - \Delta T/82.8)$.

The area under a DSC peak is related to the enthalpy change. The ratio of the sum of the areas of the second and third peaks to the area of the first peak was largest in Region C and smallest in Region B. This further implies that the smallest amount of Al–Si was present in Region C, as also indicated by consideration of ΔT.

The silicon contents determined by DSC (Tables IV and V) are consistent with those determined by X-ray diffraction (Table III).

2.2.4. Tensile testing

Tensile testing was performed using a hydraulic mechanical testing system (MTS) with a loading rate of 120 lb min^{-1} (534 N min^{-1}) at room temperature. Samples in the shape of a dog-bone were machined from the composite cylinder, with the dog-bone axis perpendicular to the axis of the composite cylinder, so the mechanical properties measured were those near the centre of the composite cylinder. However, for composites fabricated at 670 °C, tensile specimens were cut from the half-radius region, where the infiltration was more complete than the centre region. The Young's modulus was measured using a strain gauge at low loads. The ductility was determined by drawing two parallel lines marking the gauge length on the sample and measuring the distance between the lines before and after tensile testing using calipers.

Tensile stress–strain curves of Al/SiC (made with a steel mould at 780 °C) and pure aluminium are shown in Fig. 22. In contrast to the ductile aluminium matrix, Al/SiC exhibited failure strains less than 1.0%.

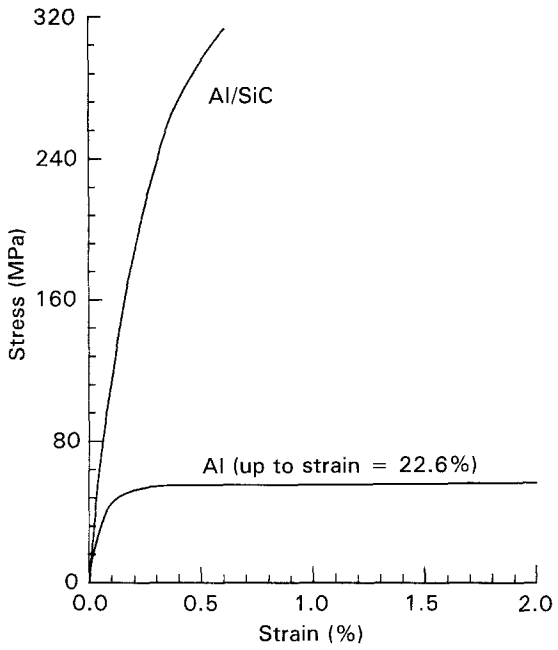

Figure 22 Tensile stress–strain curves of aluminium and Al/SiC/780 °C/st.

Table VI shows the tensile properties at room temperature of composites fabricated with either steel or graphite moulds at various infiltration temperatures. The strength and modulus were much increased and the ductility much decreased by the SiC addition. Whether steel or graphite moulds were used, the composites fabricated at all three infiltration temperatures, namely 670, 700 and 780 ± 20 °C, exhibited similar modulus values. Thus, the extent of interfacial reaction between aluminium and SiC did not change the modulus. The use of a graphite mould resulted in larger SiC consumption and a higher silicon content in the aluminium matrix but did not change the modulus of the composites. The measured modulus was larger than the theoretical value based on the Hashin and Shtrikman (H–S) model. It may be ascribed to the large aspect ratio (> 3 based on Figs 4, 5 and 8) of the SiC particles – a factor which was not considered in the H–S model. It had been shown [1] that equiaxed AlN or Al_2O_3 particulate fillers (aspect ratio = 1) gave measured moduli of the resulting composites that are close to the H–S predictions.

In the case of a steel mould used for composite fabrication, the infiltration temperature of 700 °C yielded a composite of a higher tensile strength than the infiltration temperature of 780 °C. This is ascribed to less Al–SiC reaction and a more uniform and homogeneous matrix in the composite fabricated at 700 °C. The composite fabricated at 670 °C exhibited the lowest tensile strength due to incomplete infiltration; small and uniformly distributed pores (Fig. 4) reduce the tensile strength of this composite in spite of its least severe Al–SiC reaction.

In the case where a graphite mould was used for composite fabrication, infiltration temperatures of 700 and 670 °C yielded composites of similar tensile strengths. The use of a graphite mould provided a longer time for liquid-metal infiltration and thus resulted in more complete infiltration at the half-radius region of the composite cylinder. The composite fabricated at 780 °C exhibited the lowest tensile strength due to the most severe Al–SiC reaction.

2.2.5. The interfacial shear strength distribution

A strong interfacial strength between the matrix and the reinforcement is generally desirable for composite materials. As the infiltration temperature increased, the Al–SiC interfacial reaction became more severe and resulted in a weaker interfacial shear strength due to the formation of Al_4C_3, which is brittle and moisture sensitive. The X-ray diffraction and DSC results showed a non-uniform silicon distribution in the matrix, such that the silicon content was highest in the centre of the bottom slice and lowest in the cylindrical edge region and in the top slice. This distribution is due to the silicon diffusion before aluminium matrix solidification; it does not imply that the bottom centre region had the most severe Al–SiC reaction. (The extent of the Al–SiC reaction should be constant at the same infiltration temperature if other factors, such as time, remained the same.) The Al_4C_3 concentration was highest and the SiC concentration was lowest in the edge region, indicating that the most severe Al–SiC reaction occurred in the edge region (and the top region). These phase distributions may result in non-uniform distribution of the interfacial shear strength.

TABLE VI The room-temperature tensile properties[a] of Al/SiC (55 vol % SiC) fabricated at various infiltration temperatures

Mould	Infiltration temperature (°C)	Strength (MPa)	Modulus (GPa)		Ductility (%)
			Measured	Theoretical[b]	
Steel	670	263.3 (15.4)	183.6 (2.0)	158.5	0.6 (0.1)
	700	346.7 (55.6)	186.1 (1.2)	158.5	0.8 (0.2)
	780 ± 20	313.0 (37.5)	183.4 (15.0)	158.5	0.7 (0.3)
Graphite	670	350.7 (33.5)	182.2 (4.2)	158.5	0.7 (0.1)
	700	365.1 (16.9)	184.7 (3.3)	158.5	0.7 (0.1)
	780 ± 20	294.8 (33.4)	185.6 (4.7)	158.5	0.6 (0.1)

[a] Standard deviation shown in parentheses.
[b] Hashin and Shtrikman (1963), moduli of SiC and aluminium are 440 and 62 GPa, respectively.

TABLE VII The scratch width (mm) of Al/SiC (55 vol % SiC) fabricated with steel or graphite moulds at various infiltration temperatures

Mould	Infiltration temperature (°C)	Distance from the edge of the composite cylinder				
		0 mm	5 mm	10 mm	15 mm	20 mm
Steel	670	0.55 (± 0.02)	0.54 (± 0.02)	0.65 (± 0.04)	1.19 (± 0.04)	1.23
	700	0.67 (± 0.03)	0.65 (± 0.04)	0.63 (± 0.04)	0.62 (± 0.04)	0.60
	780 ± 20	1.03 (± 0.03)	0.93 (± 0.04)	0.81 (± 0.04)	0.75 (± 0.03)	0.72 (± 0.04)
Graphite	670	0.58 (± 0.01)	0.58 (± 0.01)	0.59 (± 0.01)	0.79 (± 0.09)	1.31 (± 0.09)
	700	0.59 (± 0.00)	0.58 (± 0.01)	0.56 (± 0.01)	0.56 (± 0.02)	0.56
	780 ± 20	0.59 (± 0.02)	0.59 (± 0.01)	0.58 (± 0.02)	0.56 (± 0.04)	0.56

For interfacial shear strength testing, the shear/scratch test was performed with a Teledyne Taber Model 139 shear/scratch tester, which was equipped with a Taber S-20 contour tungsten carbide shear tool. The applied load on the tool was 1000 g. The middle slice of all composites fabricated with steel or graphite moulds at infiltration temperatures of 670, 700 or 780 ± 20 °C were tested. One or two scratches were made on the specimen surface for each increment of 5 mm from the cylindrical edge of the composite; the more uniform scratch (groove) was used for the determination of the scratch width with the help of a × 10 magnifier. The larger the scratch width, the lower was the shear strength.

Table VII shows the scratch width of composites fabricated with steel or graphite moulds at various infiltration temperatures. The graphite mould was used to avoid iron contamination, so that only the effect of the silicon distribution could be investigated. When a steel mould and infiltration temperatures of 700 and 780 °C were used, the scratch width was largest at the edge of the composite cylinder and decreased with increasing distance from the edge. For an infiltration temperature of 670 °C, the largest scratch width was observed at the centre of the composite cylinder (20 mm from the edge), whether a steel mould or a graphite mould was used; this is because of incomplete infiltration in the centre. When a graphite mould and infiltration temperatures of 700 and 780 °C were used, the scratch widths were smaller than those of composites made with a steel mould and were essentially independent of the location in the composite cylinder. Because a non-uniform silicon distribution was present in composites fabricated with a graphite mould, the uniform scratch width distribution (related to the interfacial shear strength distribution) means that the silicon distribution did not govern the shear strength distribution. In the case of composites made with a steel mould, there was not just a silicon distribution, but also an iron distribution. Thus, the non-uniform shear strength distribution in composites made with a steel mould at 700 or 780 °C is attributed to the non-uniform iron distribution. The higher iron concentration at the edge resulted in a larger scratch width or a lower shear strength, because the ternary Al–Fe–Si phase is brittle. Furthermore, for composites made with the steel mould, the scratch width increased with increasing infiltration temperature at each location in the composite cylinder.

2.2.6. Fractography

As shown in Fig. 23, the room-temperature fracture surface of Al/SiC/780 °C/st exhibited cleavage surfaces of the filler particles and microdimples in the aluminium matrix. Moreover, particle pull-out was observed, as shown by the particle (~ 5 μm in size) located in the lower half of the photograph. This indicates weak bonding between the aluminium matrix and SiC. Similar fracture morphology was also found in Al/SiC/700 °C/st and Al/SiC/670 °C/st. A similar fracture surface, except for less particle pull-out, was observed in Al/SiC/780 °C/gr (Fig. 24) compared to Al/SiC/780 °C/st (Fig. 23). This indicates that Al/SiC/780 °C/gr had stronger bonding between aluminium and SiC due to the absence of ternary Al–Fe–Si precipitates in the composite. The Al/SiC/670 °C/gr and Al/SiC/700 °C/gr composites exhibited similar fracture morphology to Al/SiC/780 °C/gr.

Fig. 25 shows the morphology at two different magnifications of the scratches at the edge and centre of the middle slice of the composite fabricated with a steel mould at 780 °C. Although both scratches showed similar morphology at a low magnification, the scratch at the edge seemed to have more cracks compared to the scratch at the centre. It was, moreover, suggested by the higher magnification photograph that more cracks and higher roughness were present in the scratch at the edge of the composite. These SEM observations are consistent with the fact that the edge of the composite had a lower shear strength than the centre.

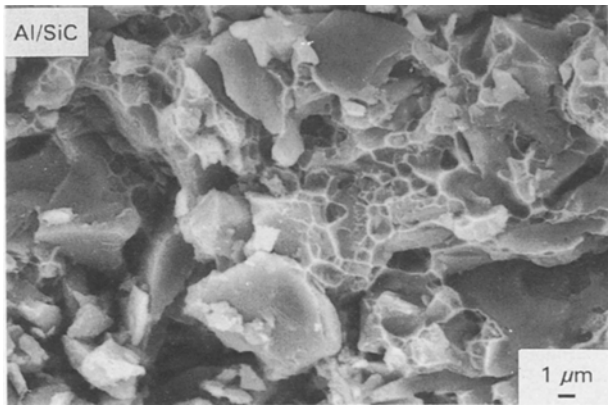

Figure 23 SEM fracture surface of Al/SiC/780 °C/st, showing particle cleavage and matrix microdimples. Particle–matrix decohesion was found in the lower centre of the photograph.

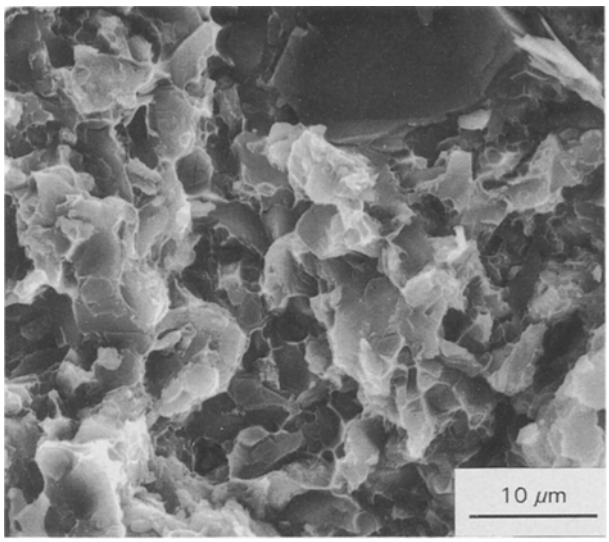

Figure 24 SEM fracture surface of Al/SiC/780 °C/gr, showing particle cleavage and matrix microdimples. No particle–matrix decohesion was found.

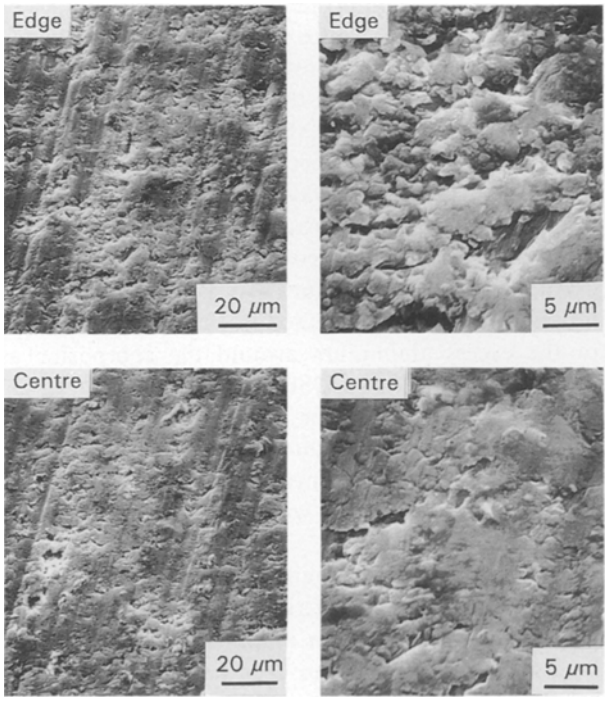

Figure 25 Scanning electron micrographs of the scratches in Al/SiC/780 °C/st in the edge and centre regions of the composite cylinder. A smoother morphology and fewer cracks were found in the centre region (bottom panels) than in the edge region (top panels). For each region, photographs at two different magnifications are shown.

3. Discussion

The SiC, silicon and Al_4C_3 phase distributions in Al/SiC fabricated by vacuum infiltration of liquid aluminium into a porous SiC particle preform held by a phosphate binder, were determined by metallography, X-ray diffraction and DSC. The silicon and SiC concentrations were highest in the part of the composite furthest away from the interface between the composite and the excess aluminium, and was lowest at the edge of the composite next to the interface. The opposite trend was observed for the Al_4C_3 distribution. Thus, the most severe Al–SiC reaction occurred in the edge and top regions, which were next to the excess aluminium. These phase distributions are due to the migration of silicon in the form of an Al–Si melt from the composite across the interface to the excess (originally liquid) aluminium. Owing to this silicon migration, the silicon concentration was highest in the part of the resulting composite furthest away from the interface between the composite and the excess aluminium. In contrast, Al_4C_3 did not migrate, as it remained a solid, so its concentration was highest in the part of the composite closest to the interface with the excess aluminium, which promoted the reaction with SiC to form Al_4C_3 and silicon. In addition, the relatively long contact time between liquid aluminium and SiC in this region enhanced the reaction. (The reaction between liquid aluminium and the graphite mould was negligible compared to that between liquid aluminium and SiC, so Al_4C_3 was not observed in the excess aluminium but only within the composite next to the excess aluminium.)

When a steel mould was used at 780 or 700 °C, facetted Al–Fe–Si (tentatively α-AlFeSi) precipitates were observed to line the above-mentioned interface on the excess aluminium side, such that the longest edge of each precipitate was on the interface. These precipitates are due to (i) the migration of silicon in the form of an Al–Si melt from the composite to the excess aluminium, (ii) the dissolving of iron from the steel mould at high temperatures, and (iii) the subsequent precipitation as various ternary Al–Fe–Si phases upon cooling by heterogeneous nucleation on the composite. In addition to the facetted Al–Fe–Si precipitates, smaller precipitates of Al–Fe–Si, Al–Fe and silicon were observed in the excess aluminium. For an infiltration temperature of 670 °C, precipitates of Al–Fe–Si and Al–Fe were observed in the excess aluminium. In the composite fabricated at 780 °C, ternary Al–Fe–Si precipitates were observed in the excess aluminium and the edge region (< 5 mm from the cylindrical edge), but not in the centre region. Thus, there was a non-uniform iron distribution, such that the iron-containing phases were present mainly in the excess aluminium, and also in the edge region. The amount of iron-containing phases increased with increasing infiltration temperature.

The effect of the non-uniform distributions of silicon and iron-containing phases on the mechanical property distribution is of practical concern. This work investigated this effect by measuring the interfacial shear strength distribution. We found that the non-uniform silicon distribution did not cause a non-uniform shear strength distribution, but the non-uniform iron distribution caused the shear strength to be lower in the edge region than the centre region of the composite cylinder. A higher iron content (as obtained by having a longer existence time of the liquid aluminium prior to solidification) caused a lower shear strength.

The SiC, silicon, Al_4C_3 and iron distributions in the Al/SiC composites of this work are related to the fact

that the composite fabrication involved the infiltration of a liquid metal. They are in contrast to the more uniform distributions in composites fabricated without liquid-metal infiltration, such as in powder metallurgy [9, 10]. The silicon migration in the former represents a dynamic situation, whereas the latter amounts to a static situation. The dynamic situation applies to vacuum infiltration, pressure infiltration, squeeze casting and other composite fabrication techniques which involve liquid-metal infiltration into a porous preform and subsequent heating before solidification, whether the liquid metal penetrates from the top or the bottom of the preform.

The silicon distribution in the Al/SiC composite cylinder was not due to macrosegregation as a result of the solidification of the binary Al–Si matrix. The following arguments provide the explanation. Firstly, macrosegregation exists when the liquid alloy becomes progressively richer in the solute as solidification progresses. The solute concentrations in a casting tend to be higher in the regions which solidify last (the centre of the ingot). However, such enrichment of the solute was arrested in Al/SiC due to the high volume fraction of fine SiC particles, which act as obstacles for the silicon movement, and also due to the ample sites for silicon nucleation as the solidification progresses. Fig. 10 shows the silicon precipitated between the SiC particles. Furthermore, no Al–Si eutectic or dendritic morphology was found in the composite. Secondly, the infiltration chamber was designed to give a lower temperature in the lower portion of the mould, so that the aluminium matrix at the bottom of the mould first solidified. If the macrosegregation had occurred, the bottom region of the composite cylinder would have contained the least amount of silicon. This is opposite to what we observed.

The infiltration temperature of 700 °C represents the optimum processing condition corresponding to a compromise between the extent of the Al–SiC reaction and the completeness of infiltration. As the infiltration temperature decreased to 670 °C, insufficient infiltration occurred in the lower middle region of the composite cylinder. This is expected to result in poor tensile properties in this region. Because the graphite mould provided a longer time for the liquid aluminium infiltrating into the SiC preform to exist before solidification for the same infiltration temperature, Al/SiC/670 °C/gr (in the mid-radius region) showed a higher tensile strength than Al/SiC/670 °C/st at the same location. It also exhibited a similar or slightly lower tensile strength than Al/SiC/700 °C/gr in the centre region. As the infiltration temperature increased to 780 ± 20 °C, the problem of incomplete infiltration was eliminated at the expense of more severe Al–SiC reaction which, in turn, decreased the tensile strength, whether steel or graphite moulds were used. The Al/SiC/780 °C/gr composite exhibited the lowest tensile strength due to the most severe Al–SiC reaction, as shown by X-ray diffraction and DSC.

At the optimum infiltration temperature of 700 °C, the presence of iron in the composite tended to decrease the tensile strength of Al/SiC. Although Al/SiC/700 °C/gr exhibited a higher silicon content (i.e. more Al–SiC reaction) throughout the composite than Al/SiC/700 °C/st, it exhibited a higher tensile strength. However, the infiltration temperature, the silicon content (i.e. the extent of the Al–SiC reaction) or the presence of iron in the matrix did not affect the tensile modulus of the composites.

In the case of a steel mould being used, the iron contamination could not be avoided. As the aluminium ingot was heated up to 750 or 800 °C for melting, the liquid aluminium readily dissolved a part of the iron from the steel mould. Contrary to the silicon out-diffusion to the surrounding excess aluminium, iron, which was dissolved in the aluminium, tended to diffuse inwards to the composite cylinder. This was evinced by the results of EDAX and SEM (Fig. 8), which show ternary Al–Fe–Si precipitate inside the edge of the composite cylinder. No effort was made to identify the phase of the ternary Al–Fe–Si phase. However, α- and β-AlFeSi were most likely because DSC results show a peak associated with the Al–α-AlFeSi eutectic melting in the edge region (< 5 mm from the cylindrical edge) and in the excess aluminium. However, no such DSC peak was observed in the centre of the composite cylinder, indicating no or very little iron in the centre of composites fabricated at all infiltration temperatures.

The contamination by the steel mould is an effect that is related to the fact that the composite fabrication involved a liquid metal. The use of a graphite mould was an effective way to avoid this contamination problem, but it also caused a more severe Al–SiC reaction throughout the composite.

Although pure aluminium was used for infiltration, no pure aluminium remained in either the composite or the excess aluminium around the composite, as shown by the lack of a DSC peak around 660 °C. All the aluminium was in the form of Al–Si of various compositions, which resulted from the Al–SiC reaction and the silicon diffusion. The average silicon concentration increased with increasing infiltration temperature.

The inferior shear strength in composites fabricated with a steel mould was attributed to the Al–SiC reaction and iron dissolution in the aluminium melt at high temperatures. Because iron has a very low solid solubility in aluminium (maximum 0.05 wt % at equilibrium), all iron in Al–Si forms second-phase particles, normally intermetallic phases of binary Al–Fe or ternary Al–Fe–Si. Because iron and silicon both have partition coefficients less than unity, most iron and silicon would segregate between dendrite arms during solidification. In addition to numerous equilibrium binary and ternary phases, a number of metastable phases readily form if the solidification condition departs from equilibrium. More than 20 intermetallic binary Al–Fe and ternary Al–Fe–Si phases have been reported [11, 12, 14, 15]. Among these, primary precipitates of Al_3Fe, α-AlFeSi, β-AlFeSi and silicon are the most likely to form during solidification. These hard and brittle precipitates are generally of sharp morphology and are undesirable because they reduce the mechanical properties of the aluminium alloy, especially in terms of the ductility

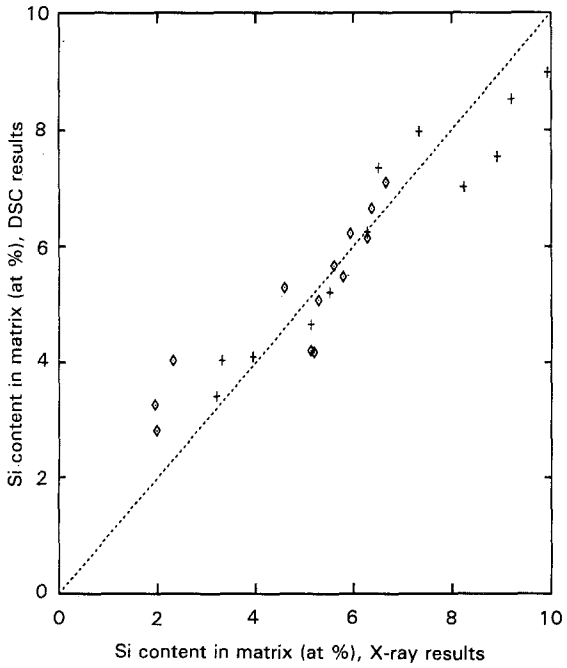

Figure 26 The correlation of the silicon contents obtained from X-ray diffraction and DSC at corresponding locations; (◇) Al/SiC, steel mould, (+) Al/SiC, graphite mould, (- - -) unity correlation.

and toughness. Although ternary Al–Fe–Si precipitates were only found in the edge region (< 5 mm from the edge of Al/SiC/780 °C/st) of the composite cylinder and iron was not detected in the inner region of the composite cylinder, the interfacial shear strength was significantly decreased even at the centre of the composite cylinder.

Both X-ray diffraction and DSC were used to characterize the localized silicon concentration throughout the composite cylinder. Fig. 26 shows the correlation of the silicon obtained from X-ray diffraction and DSC at the same corresponding location for Al/SiC composites fabricated with both steel and graphite moulds at various infiltration temperatures. The correlation was particularly good for silicon contents from 3–8 at %. For silicon contents < 3 at %, the X-ray diffraction technique gave a lower silicon content due to the fact that part of the silicon existed in the form of the Al–Si solid solution or ternary Al–Fe–Si phases, which were dissolved by the acids. For silicon contents > 8 at %, the DSC technique was less accurate due to the proximity of the matrix to the eutectic composition; a small variation in the liquidus–solidus temperature difference obtained from DSC gave a large variation in the silicon content.

4. Conclusion

This work has shown that non-uniform phase distributions exist in metal-matrix composites fabricated by liquid-metal infiltration, if the filler and the metal matrix react to form a reaction product that dissolves in the liquid metal. Because of the excess liquid metal surrounding the composite during infiltration, the reaction product that dissolves in the liquid metal outdiffuses toward the excess liquid metal. This results in a smaller concentration of this reaction product in the part of the composite next to the excess metal. In the case of SiC-reinforced aluminium, the SiC–Al reaction product that dissolves in the liquid aluminium is silicon and the non-uniform silicon distribution does not cause a non-uniform shear strength distribution.

This work has also shown that, in the case of a steel mould, non-uniform distributions of iron-containing phases exist in metal-matrix composites fabricated by liquid-metal infiltration, because the mould reacts with the liquid metal and the filler–metal reaction product dissolves in the liquid metal. The concentration of the iron-containing phases is highest in the excess metal cast around the composite and is less high within the composite. The iron-containing phases degrade the shear strength of the composite and their non-uniform distribution results in a non-uniform shear strength distribution, such that the shear strength is lower at the edge of the composite. On the other hand, in the case of a graphite mould, the reaction between graphite and liquid aluminium was negligible compared to that between SiC and liquid aluminium, so that the common reaction product, Al_4C_3, was observed only within the composite cylinder and not in the excess aluminium cast around the composite cylinder. Therefore, the composite cylinders fabricated by using a graphite mould were uniform in their shear strength distribution, in spite of their non-uniform silicon distribution.

For the fabrication of metal-matrix composites by liquid-metal infiltration such that the filler reacts with the metal, the optimum infiltration temperature is the temperature above which excessive filler–metal reaction degrades the strength of the composite, and below which infiltration is incomplete. For the case of SiC particle-reinforced aluminium fabricated by vacuum infiltration of liquid aluminium under a gas pressure, the optimum infiltration temperature is 700 °C.

Steel moulds are more thermally conductive than graphite moulds, so steel moulds used for liquid-metal infiltration give a shorter existence time of the liquid metal (prior to solidification) than graphite moulds. As a result, for composites that suffer from filler–metal reactions, the severity of the reaction is less when steel moulds rather than graphite moulds are used. However, the tendency for steel moulds to react with (or dissolve in) liquid metals makes them of limited attraction.

Acknowledgements

This work was supported by the Defense Advanced Research Projects Agency of the Department of Defense and by the Center for Electronic and Electro-Optic Materials of the State University of New York at Buffalo.

References

1. SHY-WEN LAI and D. D. L. CHUNG, *J. Mater. Sci.*, in press.
2. R. WARREN and C.-H. ANDERSON, *Composites* **15** (1984) 101.

3. T. A. CHERNYSHOVA and A. V. REBORV, *J. Less-Common Metals* **117** (1986) 203.
4. W. C. MOSHIER, J. S. AHEARN and D. C. COOKE, *J. Mater. Sci.* **22** (1987) 1154.
5. D. J. LLOYD and I. JIN, *Metall. Trans.* **19A** (1988) 3107.
6. D. J. LLOYD, H. LAGACE, A. McLEOD and P. L. MORRIS, *Mater. Sci. Eng.* **A107** (1989) 73.
7. T. ISEKI, T. KAMEDA and T. MARUYAMA, *J. Mater. Sci.* **19** (1984) 1692.
8. K. KANNIKESWARAN and R. Y. LIN, *J. Metals* **39**(9) (1987) 17.
9. J. C. VIALA, P. FORTIER, B. BONNETOT and J. BOUIX, *Mater. Res. Bull.* **21** (1986) 387.
10. H. RIBES, M. SUERY, G. L'ESPERANCE and J. G. LEGOUX, *Metall. Trans.* **21A** (1990) 2489.
11. JOHN E. HATCH (ed.), "Aluminium Properties and Physical Metallurgy" (American Society for Metals, Metals Park, OH, 1984).
12. P. R. SPERRY and M. H. BANKARO, in "Metals Handbook" 8th Edn, Vol. 8 (American Society for Metals, Metals Park, OH, 1973) p. 120.
13. J. C. VIALA, P. FORTIER and J. BOUIX, *J. Mater. Sci.* **25** (1990) 1842.
14. V. G. RIVLIN and G. V. RAYNOR, *Int. Met. Rev.* **3** (1981) 133.
15. P. SKJERPE, *Metall. Trans.* **18A** (1987) 189.
16. P. J. BLACK, *Acta Crystallogr.* **8** (1955) 43.
17. *Idem, ibid.* **8** (1955) 175.
18. R. C. HUDD and W. H. TYLER, *ibid.* **15** (1962) 441.
19. L. A. BENDERSKY, A. J. McALISTER and F. S. BIANCANIELLO, *Metall. Trans.* **19A** (1988) 2893.
20. H. KOSUGE and I. MIZUKAMI, *J. Jpn Inst. L. Metals* **22** (1972) 437.
21. C. J. SIMENSEN and R. VELLASAMY, *Z. Metallkde* **68** (1977) 428.
22. A. M. B. DOUGLAS, *Acta Crystallogr.* **3** (1950) 19.
23. E. H. HOLLINGSWORTH, G. R. FRANK Jr and R. E. WILLETT, *Trans. TMS-AIME* **224** (1962) 188.
24. L. K. WALFORD, *Acta Crystallogr.* **18** (1965) 287.
25. A. D. I. NICOL, *ibid.* **6** (1953) 285.
26. P. J. BLACK, O. S. EDWARDS and J. B. FORSYTH, *ibid.* **14** (1961) 993.
27. H. WESTENGEN, *Z. Metallkde* **73** (1982) 360.
28. R. M. K. YOUNG and T. W. CLYNE, *Scripta Metall.* **15** (1981) 1211.
29. M. COOPER, *Acta Crystallogr.* **23** (1967) 1106.
30. G. PHRAGMEN, *J. Inst. Metals* **77** (1950) 489.
31. M. COOPER and K. ROBINSON, *Acta Crystallogr.* **20** (1961) 614.
32. K. ROBINSON and P. J. BLACK, *Philos. Mag.* **44** (1953) 1392.
33. P. LIU, T. THORVALDSSON and G. L. DUNLOP, *Mater. Sci. Tech.* **2** (1986) 1009.
34. A. L. DONS, *Z. Metallkde* **75** (1984) 170, 609.
35. M. ARMAND, "Congres International de L'aluminium", Paris, Vol. 1 (1954) pp. 305–27.
36. D. MUNSON, *J. Inst. Metals* **95** (1967) 217.
37. W. JANICHE, *Aluminium Arch.* **5** (1936) 21.
38. P. K. PANDAY and K. SCHUBERT, *J. Less-Common Metals* **18** (1969) 175.
39. C. J. SIMENSEN, P. FARTUM and A. ANDERSEN, *Fres. Z. Anal. Chem.* **319** (1987) 286.

Received 8 March
and accepted 30 November 1993